Enhancement of Reservoir Computing Performance via Ultrashort Optical Feedback

Ting Li(李婷)[1], Zebin Li(李泽彬)[1], Chenpeng Xue(薛琛鹏)[1,*], Zuxing Zhang(张祖兴)[1], and Yanhua Hong[2]

[1]*College of Electronic and Optical Engineering, College of Flexible Electronics (Future Technology), Nanjing University of Posts and Telecommunications, Nanjing 210023, China*

[2]*School of Computer Science and Engineering, Bangor University, Bangor LL57 1UT, UK*

An enhanced delay-based photonic reservoir computing system assisted by ultrashort optical feedback is proposed and numerically demonstrated. Specifically, a picosecond-scale ultrashort optical feedback loop is integrated into a conventional semiconductor laser-based single-feedback reservoir computing (RC) architecture. The ultrashort feedback loop acts as a fast dynamical regulator, enabling multiscale temporal dynamics while largely preserving the structural simplicity of the single-feedback configuration. The RC performance is evaluated in terms of separability and consistency. The results show that appropriately selected ultrashort feedback parameters can increase between-class separation and reduce within-class dispersion while maintaining reproducible reservoir responses. Moreover, the memory capacity performance and benchmark evaluations using Santa Fe chaotic time-series prediction and nonlinear channel equalization demonstrate that the proposed system outperforms the conventional single-feedback reservoir.

Keywords: photonic reservoir computing, semiconductor laser, ultrashort optical feedback, state separability, reservoir consistency

PACS: 42.62.-b, 05.45.-a

1. Introduction

Reservoir computing (RC), originating from Recurrent Neural Networks (RNNs), is an efficient information processing paradigm based on nonlinear dynamical systems. It utilizes the transient response of complex systems to process time-dependent tasks and requires only the training of a linear readout layer.[1-3] By eliminating the backpropagation training for internal connection weights, RC demonstrates excellent stability and computational efficiency in modeling complex nonlinear dynamics and time-series tasks.

In recent years, the increasing demand for high-speed and low-power information processing, as well as high-accuracy pattern recognition, has driven significant interest in delay-based photonic reservoir computing (DPRC),[4-8] due to its structural simplicity and high experimental feasibility. A typical DPRC system comprises a physical nonlinear element combined with an optical feedback loop, where a

* Corresponding author. E-mail: cp_xue@njupt.edu.cn

high-dimensional network of virtual nodes is implemented through time-multiplexing.[9-11] Numerous studies have demonstrated that DPRC can achieve performance comparable to, or even superior to, conventional neural networks in tasks such as chaotic time-series prediction, nonlinear channel equalization, and pattern recognition.[12-16] Various architectural approaches have also been investigated to improve DPRC performance. For instance, the nonlinear dynamics of the system can be enhanced by introducing multiple feedback loops,[17,18] the diversity of virtual node states can be improved through optimized input masking strategies,[19] and the linear memory capacity (MC) can be strengthened by constructing multi-delay architectures.[20] These approaches have achieved certain improvements in RC performance.

Previous studies on semiconductor laser dynamics have shown that the external cavity delay is a key parameter governing the dynamical behavior of the system.[21,22] Even in the short external cavity regime, optical feedback can significantly influence the nonlinear response of the laser.[23] Furthermore, the coexistence of feedback loops with different timescales can effectively reshape the overall dynamical structure of delay-coupled laser systems.[24] However, the combined use of long and short feedback loops in RC has received limited attention.

In this work, we propose a high-performance delay-based photonic reservoir computing system assisted by ultrashort optical feedback (DPRC-UOF). The proposed system is analyzed in terms of separability and consistency, and its computational capability is further validated using benchmark tasks. The remainder of this paper is organized as follows. Section 2 introduces the proposed system and its mathematical model. Section 3 analyses the separability and consistency of the reservoir states. Section 4 evaluates the proposed architecture using Santa Fe chaotic time-series prediction, nonlinear channel equalization and memory capacity (MC) task. Finally, Section 5 presents the conclusion.

2. Principles and system model

Fig. 1 shows the schematic of the proposed DPRC-UOF system. In the input layer, during each input period T, the input signal $u(n)$ is multiplied by a mask signal $m(t)$ and scaled to generate the driving signal for the phase modulator, $s(t) = u(n)\times m(t)\times\gamma$, where n denotes the discrete time index and γ is the scaling factor. Then the modulated signal is injected into the reservoir.[25] The reservoir consists of a response semiconductor laser (RSL) with two optical feedback loops characterized by substantially different delay times: a long optical feedback loop and a picosecond-scale ultrashort optical feedback (UOF) loop. This configuration differs significantly from conventional dual-delay reservoir architectures with comparable delay times.[18] As the main feedback delay, the long delay has a delay of $\tau_1 = T+\theta$, ensuring that the states of all virtual nodes associated with the current input are fed back into the RSL while preventing interference with the next input period.[26-28] The UOF (i.e. $\tau_2 < 0.1$ ns) provides additional fast-timescale dynamical modulation that regulates the reservoir states. Consequently, multiscale temporal dynamics are introduced while the structural simplicity of the system is largely preserved. The

reservoir output $y(n)$ is calculated as a linear combination of the virtual nodes $x_i(n)$ (i = 1, 2, 3, …, N) and their corresponding readout weights W_i, as expressed by:

$$y(n) = \sum_{i=1}^{N} W_i x_i(n) \tag{1}$$

It serves as the read-out estimator, and the output weights are optimized using ridge regression to minimize the mean square error between the target values $\bar{y}(n)$ and $y(n)$.

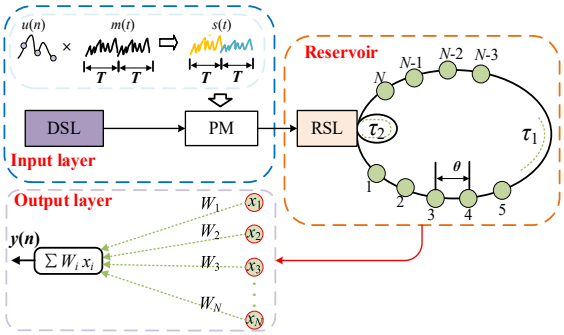


Fig. 1. Schematic diagram of DPRC-UOF. RSL: response semiconductor laser, DSL: driving semiconductor laser, PM: phase modulator.

The proposed system can be modelled using the following Lang-Kobayashi equations:[16, 18]

$$\begin{aligned}\frac{\mathrm{d}E(t)}{\mathrm{d}t} = \frac{1+\alpha}{2}\left[g\frac{\quad t)-N_0}{1+\varepsilon\quad}-\frac{1}{\tau_{\quad}}\right]E(t)+k_1E\left(t-\tau\quad\right)\\ +k_2E\left(t-\tau\quad\right)+\kappa_{\mathrm{inj}}E_{\mathrm{inj}}(t)e^{i2\pi\Delta\nu t}+f(t)\end{aligned} \tag{2}$$

$$\frac{\mathrm{d}N(t)}{\mathrm{d}t} = J-\frac{N(t)}{\tau_{\mathrm{s}}}-g\frac{N(t)-N_0}{1+\varepsilon\left|E(t)\right|^2}\left|E(t)\right|^2 \tag{3}$$

where $E(t)$ and $E_{\mathrm{inj}}(t)$ are the complex electric fields of the RSL and the driving semiconductor laser (DSL). $N(t)$ is the corresponding carrier density, and N_0 is the carrier density at transparency. k_1 and τ_1 (k_2 and τ_2) are the strength and delay time of the long (ultrashort) feedback loop, respectively. k_{inj} is the injection strength, α is the linewidth enhancement factor, g is the differential gain coefficient, and ε denotes the gain saturation coefficient. ν is the frequency of RSL, and $\Delta\nu$ is the frequency detuning between DSL and RSL. τ_{p} is the photon lifetime, τ_{s} is the carrier lifetime. J is the injection current. $f(t)$ represents the white Gaussian noise. In our simulation, the signal-to-noise ratio (SNR) of the RSL was set to 20 dB,[18] unless stated otherwise. $E_{\mathrm{inj}}(t)$ is given by the following equation,

$$E_{\mathrm{inj}}(t) = \sqrt{I_{\mathrm{d}}}e^{\mathrm{i}\pi s(t)} \tag{4}$$

where I_{d} is the light intensity of the steady state of the DSL.

Equations (2)-(3) are solved using the fourth-order Runge–Kutta method with a time step of 1 ps. The parameters are set as follows: $\alpha = 3.0$, $g = 8.4\times10^{-13}$ m^3s^{-1}, $N_0 = 1.4\times10^{24}$ m^{-3}, $\varepsilon=2.0\times10^{-23}$, $\tau_p = 1.927$ ps, $\tau_s = 2.04$ ns, $k_{inj} = 12.43$ ns^{-1}, $\nu = 1.96\times10^{14}$ Hz, $\Delta\nu = -4.0$ GHz, $J = 1.037\times10^{33}$ m^3s^{-1}, $I_d = 6.56\times10^{20}$, and $k_1 = 15.53$ ns^{-1}. In the simulations, we set $T = 1$ ns, $N = 100$, $\theta = T/N$, $\gamma = 0.6$, and $\tau_1 = T+\theta$. Meanwhile, a chaotic signal with peak frequency 5.7 GHz, standard deviation 1, and mean value 0 is used as the mask signal. To prevent overfitting, the ridge regression parameter λ is set to 1×10^{-6}.[29]

3. Reservoir State Analysis

An effective reservoir should satisfy two requirements. First, different inputs should be mapped into sufficiently distinguishable reservoir states.[9, 11] Second, the reservoir should produce consistent and reproducible responses when the same input is repeatedly presented.[30]

3.1. Separability

The separability of reservoir states determines how distinguishable different inputs are in the high-dimensional state space, thereby directly affecting the ability of the linear readout layer to extract target information. Here, the separability is quantified using a Fisher discriminant ratio F,[31-33] which is defined as follows:

$$F = \frac{\mathrm{tr}(\boldsymbol{S}_b)}{\mathrm{tr}(\boldsymbol{S}_w)} \tag{5}$$

where tr(·) is the trace of matrix, $\boldsymbol{S}_b$ and $\boldsymbol{S}_w$ are the between-class and within-class scatter matrices, respectively, and are defined as follows:

$$\boldsymbol{S}_b = \sum_{c=1}^{C} n_c(\boldsymbol{\mu}_c - \boldsymbol{\mu})(\boldsymbol{\mu}_c - \boldsymbol{\mu})^T \tag{6}$$

$$\boldsymbol{S}_w = \sum_{c=1}^{C}\sum_{j=1}^{n_c}(\boldsymbol{x}_{c,j} - \boldsymbol{\mu}_c)(\boldsymbol{x}_{c,j} - \boldsymbol{\mu}_c)^T \tag{7}$$

where $\boldsymbol{\mu}$ is the overall mean state vector, C is the number of classes, $\boldsymbol{\mu}_c$ is the mean state vector of the c-th class, and n_c is the number of samples in the c-th class. The vector $\boldsymbol{x}_{c,j} \in \mathbf{R}^N$ denotes the j-th reservoir-state sample in the c-th class, where $c = 1, 2, \ldots, C$ and $j = 1, 2, \ldots, n_c$. Specifically, $\boldsymbol{x}_{c,j} = [x_{c,j,1}, x_{c,j,2}, x_{c,j,3},\ldots x_{c,j,N}]^T$, whose components represent the states of the N virtual nodes. The $\mathrm{tr}(\boldsymbol{S}_b)$ characterizes the overall separation between the centers of different input classes in the reservoir state space. A larger $\mathrm{tr}(\boldsymbol{S}_b)$ indicates greater separation between the class means. In contrast, $\mathrm{tr}(\boldsymbol{S}_w)$ characterizes the dispersion of samples within each class. A smaller $\mathrm{tr}(\boldsymbol{S}_w)$ indicates that samples belonging to the same class are more tightly clustered in the reservoir state space.

Fig. 2 presents the evolutions of $\mathrm{tr}(\boldsymbol{S}_b)$, $\mathrm{tr}(\boldsymbol{S}_w)$ and F versus τ_2 and k_2. Here, $u(n)$ is randomly chosen from {-3, -1, 1, 3}, corresponding to $C = 4$. The parameters of the long feedback loop are set to $k_1 = 15.53$ ns^{-1} and $\tau_1 = 1.01$ ns. The nominal long-feedback parameters are fixed here to isolate the influence of the UOF parameters and identify a favorable UOF operating region. After the first 200 transient

samples are discarded, the remaining 3800 reservoir-state samples are grouped into four classes according to their corresponding input-symbol labels ($\sum_{c=1}^{4} n_c = 3800$). As shown in Fig. 2(a), when τ_2 and k_2 are in the ranges of 20 - 60 ps and 1 - 25 ns^{-1}, respectively, tr($\boldsymbol{S}_b$) of the DPRC-UOF can exceed 1.5×10^5, which is higher than the value obtained without UOF (~1.18×10^5). The boundary of the τ_2 can be attributed to that τ_2 < 60 ps yields an external-cavity free spectral range (FSR) over 16.67GHz, which is far away from the that of long feedback loop and the relaxation oscillation frequency (~5.7 GHz). Therefore, it would not lead to significantly coherence collapse.[34] Moreover, the system may also lose stability when τ_2 becomes comparable to the photon lifetime (2.04 ps). Fig. 2(b) corresponds to the evolution of tr($\boldsymbol{S}_w$). Clearly, relatively low tr($\boldsymbol{S}_w$) are also obtained within the same parameter region and are lower than the value obtained without UOF (~2.62×10^5). As a result, a region with high F area (>0.75) is observed in Fig. 2(c), substantially exceeding the value obtained without UOF (0.452). These results show that the separability of the reservoir states can be improved by appropriately selecting the UOF parameters.

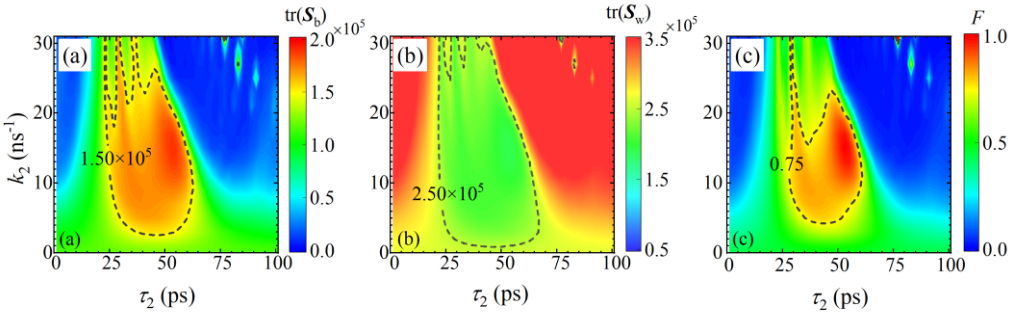


Fig. 2. Separability as functions of τ_2 and k_2, (a) tr($\boldsymbol{S}_b$), (b) tr($\boldsymbol{S}_w$) and (c) F. k_1 = 15.53 ns^{-1} and τ_1 = 1.01 ns.

Fig. 3 presents the evolution of F as a function of k_1 and τ_1, respectively. Here k_2 = 15 ns^{-1} and τ_2 = 50 ps are selected as representative operating parameters based on the favorable UOF parameter region identified above. A weak k_1 degrades the performance of the RC,[35] and the RC would be dominated by the relatively strong UOF. Therefore, k_1 is set in the range of 7 ns^{-1} - 23 ns^{-1}. Apparently, the proposed DPRC-UOF consistently achieves higher F values than the conventional DPRC without UOF throughout this range. The inset of Fig. 3 shows F evolution as a function of τ_1 (Here N is fixed to 100, but θ is changed). The proposed DPRC-UOF maintains higher F values than the conventional DPRC when τ_1 is in the range of 0.5 - 10 ns. However, F decreases as τ_1 is increased further. These results indicate that the proposed DPRC-UOF is relatively robust against variations in the long feedback loop parameters within the investigated ranges.

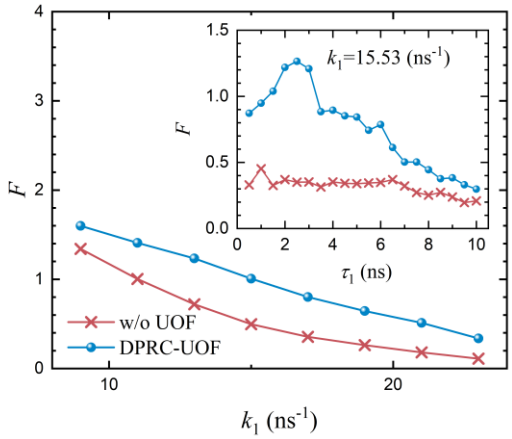


Fig. 3. F as a function of k_1 with τ_1 = 1.01 ns, the inset is F as a function of τ_1 with k_1 = 15.53 ns^{-1}.

3.2. Consistency

Consistency is defined as the reproducibility of the response waveforms of a nonlinear dynamical system when it is driven repeatedly by the same input signal under different initial conditions. For simplicity, two independent simulations with the same input signal are performed under different initial conditions. Consistency is quantified using two metrics: the node correlation coefficient (CC) and the relative root mean square error (RelRMSE), which are defined as follows:[30, 36, 37]

$$CC = \frac{\left\langle \left(x^{(1)} - \left\langle x^{(1)} \right\rangle \right) \left(x^{(2)} - \left\langle x^{(2)} \right\rangle \right) \right\rangle}{\sigma\left(x^{(1)} \right) \sigma\left(x^{(2)} \right)} \tag{8}$$

$$\mathrm{RelRMSE} = \frac{\left\| \boldsymbol{X}^{(1)} - \boldsymbol{X}^{(2)} \right\|_{\mathrm{F}}}{\left\| \boldsymbol{X}^{(1)} \right\|_{\mathrm{F}}}. \tag{9}$$

where $x^{(k)}$ denotes the whole node sequence in the k-th simulation (k=1, 2), σ denotes the standard deviation of the target sequence, $\boldsymbol{X}^{(k)} = [x_i(n)^{(k)}] \in \mathrm{R}^{M \times N}$ denotes the reservoir-state matrix, $x_i(n)^{(k)}$ is the virtual node corresponding to the k-th simulation, M is the number of valid input samples (here, M = 3800), and $\|\cdot\|_{\mathrm{F}}$ represents the Frobenius norm. A large CC (close to 1) and a small RelRMSE indicate highly consistent reservoir responses.

Fig. 4 shows the evolutions of CC and RelRMSE as functions of τ_2 and k_2. As shown in Fig. 4(a), when k_2 <10 ns^{-1}, CC > 0.99 is maintained over the entire investigated range of τ_2 (1 – 100 ps). As k_2 increases beyond 10 ns^{-1}, the range of τ_2 over which CC>0.99 is achieved gradually narrows. For instance, when k_2 = 20 ns^{-1}, CC > 0.99 is achieved only for τ_2 between 10 ps and 47 ps. However, the CC results alone do not clearly demonstrate the superiority of the proposed DPRC-UOF, since CC > 0.99 is also achieved in the case without UOF (Seeing k_2 = 0 ns^{-1}). Fig. 4(b) shows that, within the region enclosed by the black dashed contour, the RelRMSE of the proposed DPRC-UOF remains below 1.2×10^{-6}. It is noted that without UOF (k_2 = 0 ns^{-1}), the RelRMSE is 1.25×10^{-6}. These results indicate that, within the identified

parameter region, the proposed DPRC-UOF achieves higher consistency than the conventional DPRC without UOF.

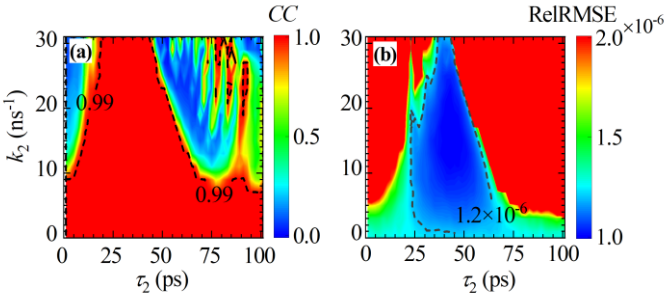


Fig. 4. Consistency of the DPRC-UOF as a function of τ_2 and k_2, (a) *CC* and (b) RelRMSE with k_1 = 15.53 ns^{-1} and τ_1 = 1.01 ns.

Fig. 5 shows the RelRMSE of the proposed DPRC-UOF and the conventional DPRC without UOF as functions of k_1. With k_2 = 15 ns^{-1} and τ_2 = 50 ps, when k_1 < 21 ns^{-1}, both systems maintain RelRMSE values on the order of 10^{-6}. However, the proposed DPRC-UOF consistently exhibits lower RelRMSE values than the conventional DPRC without UOF, indicating better consistency. The inset in Fig 5 shows the RelRMSE as a function of τ_1. Similarly, the DPRC-UOF maintains lower RelRMSE values than the conventional DPRC without UOF over the investigated range of τ_1. Moreover, when τ_1 > 6 ns, the RelRMSE increases with increasing τ_1, leading to a slight degradation in consistency. Overall, these results demonstrate that the consistency of the proposed DPRC-UOF is relatively robust to the parameter settings of the long feedback loop.

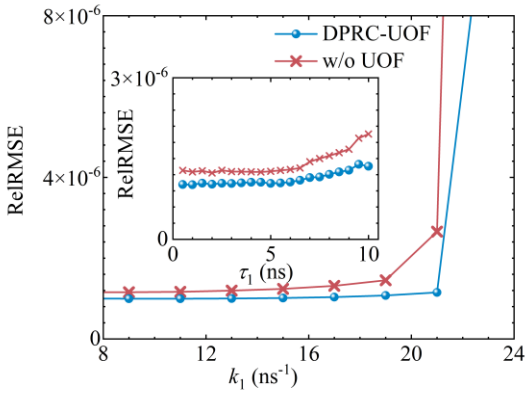


Fig. 5. RelRMSE as a function of k_1 with τ_1 = 1.01 ns; the inset is RelRMSE as a function of τ_1 with k_1 = 15.53 ns^{-1}.

4. Task Evaluation

To assess the practical information processing performance of the proposed system, the well-known Santa Fe chaotic time-series prediction task and nonlinear channel equalization task are employed as benchmarks.[19, 38]

4.1. Santa Fe chaotic time-series prediction task

Briefly, 3000 samples from the Santa Fe chaotic time-series are used for training and

a further 1000 samples are used for testing.[18, 28] The prediction performance is quantified using the normalized mean square error (NMSE), defined as:

$$\mathrm{NMSE} = \frac{\left\langle \left(\bar{y}(n) - y(n)\right)^2 \right\rangle}{\sigma^2(\bar{y}(n))} \tag{10}$$

where $y(n)$ is the prediction result of the RC system, and $\bar{y}(n)$ is the corresponding target value.

Fig. 6 shows the variation of the NMSE with respect to τ_2 and k_2. Clearly, NMSE < 0.013 can be achieved by properly setting the UOF parameters within the region enclosed by the white dashed contour. Notably, the parameter region associated with a low NMSE is consistent with the results of the separability and consistency analysis.

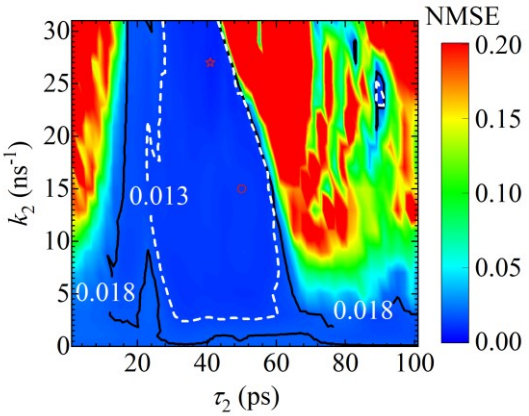


Fig. 6. Distribution of NMSE for the Santa Fe time-series prediction task as a function of τ_2 and k_2,
the star marks the operating point with k_2 = 27 ns^{-1} and τ_2 = 41 ps, while the circle indicates k_2 = 15 ns^{-1} and τ_2 = 50 ps.

For the conventional DPRC without UOF, the NMSE is 0.0184. When with k_2 = 15 ns^{-1}and τ_2 = 50 ps, the NMSE is ~ 0.0115. When with k_2 = 27 ns^{-1} and τ_2 = 41 ps, the NMSE is further reduced to 0.0065. Figs. 7(a1)-(b2) show the performance of the system in the Santa Fe chaotic time-series prediction task. Clearly, with k_2 = 27 ns^{-1}and τ_2 = 41 ps, the predicted sequence agrees much more closely with the target sequence, and the local peaks in the prediction error are substantially reduced relative to that without UOF. Fig. 7(c) shows the NMSE evolution as a function of k_1, obtained by averaging over 10 independent simulations. When k_1 < 23 ns^{-1}, the NMSE of the DPRC-UOF decreases with increasing k_1 and remains lower than that of the conventional DPRC without UOF. When k_1 exceeds 23 ns^{-1}, the NMSE of both systems increases rapidly. Moreover, as shown in the inset, the DPRC-UOF achieves a lower NMSE than the conventional DPRC when τ_1 < 8 ns. Overall, these results demonstrate that the introduction of UOF can significantly improve the Santa Fe time-series prediction performance with appropriately chosen feedback parameters.

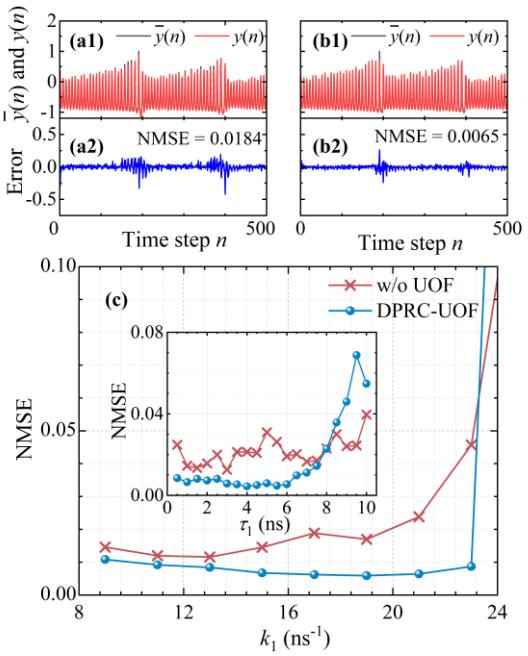


Fig. 7. Prediction results of the Santa Fe chaotic time-series task. (a) without UOF. (b) DPRC-UOF, $k_2 = 27$ ns^{-1} and $\tau_2 = 41$ ps. the black, red and blue curves denote the target, predicted, and error signals, respectively. (c) NMSE as a function of k_1 with $\tau_1 = 1.01$ ns; the inset shows NMSE versus τ_1 with $k_1 = 15.53$ ns^{-1}.

4.2. Nonlinear channel equalization task

Next, the nonlinear channel equalization task is employed to further evaluate the performance of the proposed DPRC-UOF. The objective of this task is to recover the input symbol $d(n)$ from the received signal $m(n)$ transmitted through a standardized nonlinear multipath RF channel, affected by multipath propagation, nonlinear distortion and additive noise.[37] The received sequence $m(n)$ is aligned with the target symbol $d(n)$ during the numerical implementation, and no additional equalization delay is introduced. The input symbols $d(n)$ are randomly chosen from {-3, -1, 1, 3} and the channel model is defined as follows:[19]

$$\begin{aligned} q(n) = {} & 0.08d(n+2) - 0.12d(n+1) + d(n) + 0.18d(n-1) \\ & -0.1d(n-2) + 0.091d(n-3) - 0.05d(n-4) \\ & +0.04d(n-5) + 0.03d(n-6) + 0.01d(n-7) \end{aligned} \tag{11}$$

$$m(n) = q(n) + 0.036q^2(n) - 0.011q^3(n) + \xi(n) \tag{12}$$

where $\xi(n)$ is a Gaussian noise with zero mean, adjusted to yield signal-to-noise ratios (SNRs) ranging from 12 dB to 32 dB.

Fig. 8 shows the effect of τ_2 and k_2 on the symbol error rate (SER) in the nonlinear channel equalization task. Here, SER is defined as the ratio of the number of incorrectly recovered symbols to the total number of test symbols. After the continuous readout output is obtained, each output value is mapped to the nearest symbol in the set {-3, -1, 1, 3}. The recovered symbols are then compared with the corresponding target symbols to calculate the SER. The SNR is set to 20 dB, and 9000

symbols are generated, of which 3000 samples are used for training and 6000 for testing.[39] As shown by the white dashed contour, the SER of the proposed DPRC-UOF is less than 0.048, which is lower than that of the conventional DPRC without UOF (~0.049 with k_2=0 ns^{-1}). Furthermore, within the red dashed contour, SER < 0.024 is achieved. For instance, with k_2 = 15 ns^{-1}and τ_2 = 50 ps, the SER is ~0.025, while with k_2 = 27 ns^{-1}and τ_2 = 41 ps, the SER is ~0.023. Notably, the low-SER region is also consistent with the parameter region exhibiting enhanced separability and consistency, as shown in Figs. 2 and 4. Overall, these results demonstrate that the introduction of UOF can significantly improve the nonlinear channel equalization performance of the reservoir computing system.

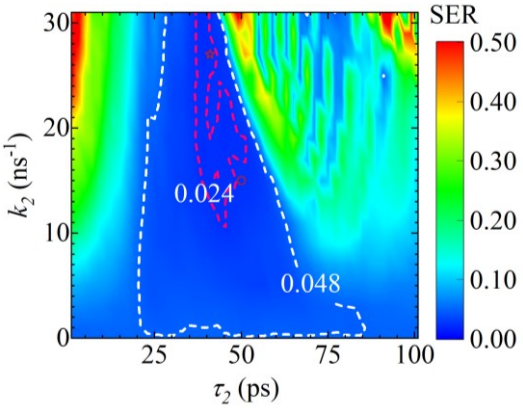


Fig. 8. SER as a function of τ_2 and k_2, the star marks the operating point with k_2 = 27 ns^{-1} and τ_2 = 41 ps, while the circle indicates k_2 = 15 ns^{-1} and τ_2 = 50 ps.

Fig. 9(a) presents the SER evolution as a function of k_1, with the SNR fixed at 20 dB. The SER values shown in Fig. 9(a) and Fig. 9(b) are obtained by averaging over 10 independent simulations. As k_1 increases, the SER of the proposed DPRC-UOF decreases, reaching a minimum at k_1 = 15 ns^{-1}, and then it increases. For the conventional DPRC without UOF, the SER remains nearly constant (SER ~ 0.035) over the range of 7 ns^{-1} < k_1 < 11 ns^{-1}. When k_1 exceeds 11 ns^{-1}, the SER increases with increasing k_1. It is worth noting that, throughout the investigated range of k_1 (7 ns^{-1} - 25 ns^{-1}), the proposed DPRC-UOF consistently achieves a lower SER than the conventional DPRC without UOF. Moreover, it maintains a SER<0.03 for 7 ns^{-1} < k_1 < 21 ns^{-1}. The inset of Fig. 9(a) shows the SER versus τ_1. Clearly, the DPRC-UOF outperforms the conventional DPRC without UOF over the entire investigated range of τ_1 (0.5 ns - 10 ns). Fig. 9(b) presents the SER as a function of the SNR. As the SNR increases, the SER of both systems gradually decreases. However, the proposed DPRC-UOF consistently achieves a lower SER than the conventional DPRC without UOF across the entire investigated SNR range, demonstrating its superior nonlinear channel equalization performance.

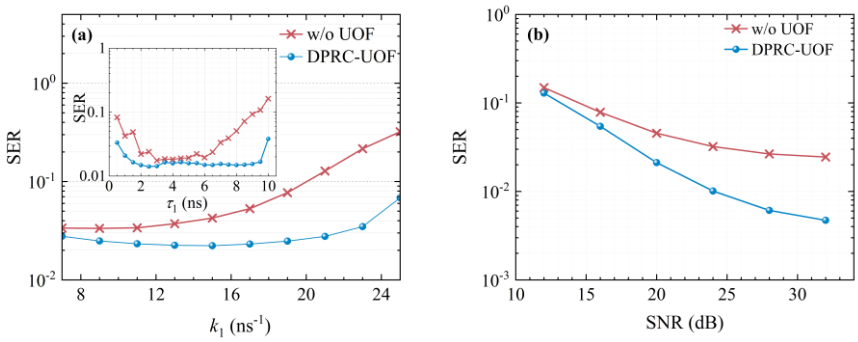


Fig. 9. SER evolution as a function of, (a) k_1 with $\tau_1 = 1.01$ ns, and (b) SNR with $k_1 = 15.53$ ns^{-1}, $\tau_1 = 1.01$ ns, $k_2 = 27$ ns^{-1} and $\tau_2 = 41$ ps, the inset in (a) is SER versus τ_1 with $k_1 = 15.53$ ns^{-1}.

4.3. MC task

Here, the linear memory capacity (LMC) and the quadratic memory capacity (QMC) are used to evaluate its ability to reproduce the past input signals and their higher-order Legendre polynomials, respectively, which are quantified by [40]

$$\mathrm{LMC} = \sum_{i=1}^{\infty} \frac{\langle u(n-i)y(n)\rangle^2}{\sigma^2[u(n)]\sigma^2[y(n)]} \tag{13}$$

$$\mathrm{QMC} = \sum_{i=1}^{\infty} \frac{\langle [3u^2(n-i)\text{-}1]y(n)\rangle^2}{\sigma^2[3u^2(n)\text{-}1]\sigma^2[y(n)]} \tag{14}$$

For the DPRC without UOF, with $k_1 = 15.53$ ns^{-1} and $\tau_1 = 1.01$ ns, the LMC and QMC are calculated as 3.626 and 1.594, respectively. The ΔLMC and ΔQMC are defined as the increment of LMC and QMC relative to the DPRC without UOF. Fig. 10 (a) and (b) show the evolutions of ΔLMC and ΔQMC as a function of k_2 and τ_2 respectively. Clearly, a positive ΔLMC can be achieved when the τ_2 is in the range ~ 20-60 ps. Similar results are also observed in the ΔQMC evolution. Moreover, a relatively large k_2 (> 25 ns^{-1}) is detrimental to ΔLMC, but can still be used to achieve positive ΔQMC, particularly when 30 ps <τ_2 < 45 ps. Notably, the ranges for positive ΔLMC and ΔQMC are similar to those observed for the separability, consistency, and benchmark task performance investigated in Figs. 2, 4 ,6 and 8.

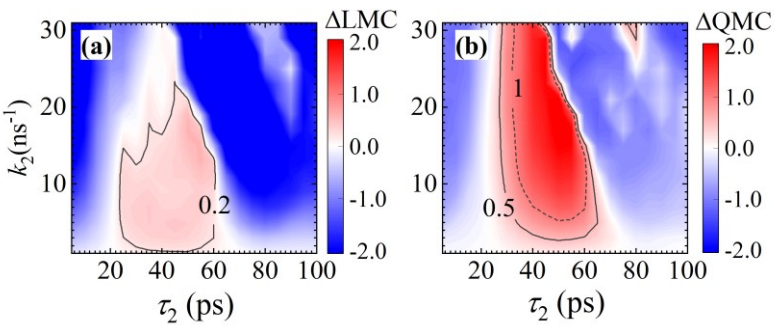


Fig. 10 Evolutions of the ΔLMC (a) and ΔQMC (b) as a function of k_2 and τ_2

Fig. 11 shows the LMC and QMC as a function of the k_1. Here, two DPRC-UOF

configurations with (k_2=15 ns^{-1}, τ_2=50 ps) and (k_2=27 ns^{-1}, τ_2= 41 ps) are studied and compared with the counterpart without UOF. As shown in Fig. 11(a), with k_1 increases, LMC in all three cases initially rises and reaches its maximum near the destabilization point [See the insets in Fig. 11(a)]. The LMC values then decrease upon further increasing k_1. Notably, the cases of DPRC with UOF can both hold a much larger LMC than that without UOF. As for the QMC, as shown in Fig. 11(b), the two cases of DPRC with UOF can still hold lager QMCs than that without UOF. Therefore, the introduction of UOF yields a better capability to reconstruct the linear components of past input signals and capture the second-order nonlinear correlations of historical inputs.

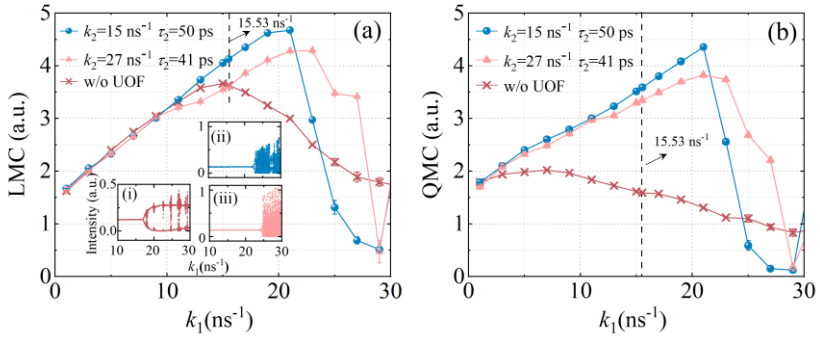


Fig. 11 LMC (a) and QMC (b) versus k_1, the insets (i)-(iii) are corresponding to the bifurcations of RC without UOF, with (k_2=15 ns^{-1}, τ_2=50 ps) and (k_2=27 ns^{-1}, τ_2= 41 ps) respectively.

The picosecond-scale UOF loop could in principle be implemented using a compact external optical path or an integrated optical waveguide, and the feedback strength can be adjusted through optical attenuators.[41] In practice, the component and fabrication tolerances may cause deviations in the effective τ_2 and k_2 from their nominal values. Our investigation present that the RC performance is robust to the τ_2 and k_2 to some extent. Moreover, the feedback phase is kept fixed, therefore, the influence of independent phase fluctuations is beyond the scope of the present work. Experimental implementation of the proposed architecture and a more comprehensive investigation of its robustness under realistic experimental imperfections will be pursued in future work.

5. Conclusions

This work proposes a high-performance delay-based photonic RC architecture by integrating a picosecond-scale ultrashort optical feedback loop into a conventional single-feedback reservoir system. The embedded ultrashort loop acts as a fast dynamical regulator (enabling multiscale temporal dynamics). It can effectively reshape the reservoir state space and enhance the system's ability to capture complex nonlinear dynamical features, while largely preserving the structural simplicity of the conventional single-feedback designs. A systematic analysis of the reservoir states confirms that ultrashort feedback enhances both state separability and operational

consistency within an appropriate parameter range, thereby improving the information-processing capability of the system. The effective performance of the proposed architecture is further verified using two standard RC benchmark tasks. For Santa Fe chaotic time-series prediction, optimized ultrashort feedback reduces the NMSE from 0.0184 for the conventional DPRC to 0.0065 for the proposed DPRC-UOF. In the nonlinear channel equalization task, the proposed DPRC-UOF achieves a SER below 0.024, compared with approximately 0.049 for the conventional DPRC without UOF. Notably, the parameter regions yielding improved performance closely coincide with those exhibiting enhanced state separability and consistency. These results indicate that the richer dynamics RC with the aid of ultrashort optical feedback can facilitate the separability by mapping of scalar inputs into higher-dimensional dynamics, improve state consistency, and consequently enhances prediction capabilities. Moreover, the MC study presents that with appropriate feedback parameters (UOF) and relatively strong feedback strength in the long feedback loop, the LMC and QMC can be improved effectively, which indicting a better capability to process past input signals and implement second-order nonlinear transformations of delayed inputs. Therefore, incorporating a properly optimized picosecond-scale ultrashort feedback loop provides an effective and structurally simple approach to enhancing the computational capacity of delay-based photonic reservoir computing.

Data availability statement

The data that support the findings of this study are available from the corresponding author upon reasonable request.

Acknowledgment

This work was supported in part by the National Natural Science Foundation of China (Grant No. 62175116).

References

[1] Jaeger H and Haas H 2004 *Science* **304** 78
[2] Lukoševičius M and Jaeger H 2009 Comput. *Sci. Rev.* **3** 127
[3] Tang J, Xia L, Li G, Fu J, Duan S and Wang L 2024 *Chin. Phys. B*, 33 037302.
[4] Tanaka G, Yamane T, Héroux J B, Nakane R, Kanazawa N, Takeda S, Numata H, Nakano D and Hirose A 2019 *Neural Netw.* **115** 100
[5] Wang D L, Nie Y K, Hu G L, Tsang H K and Huang C R 2024 *Nat. Commun.* **15** 10841
[6] Zhong D Z, Xu Z, Hu Y L, Zhao K K, Zhang J B, Hou P, Deng W A and Xi J T 2022 *Chin. Phys. B* **31** 074205
[7] Guo X X, Zhou H X, Xiang S Y, Yu Q, Zhang Y H, Han Y N and Hao Y 2024 *ACS Photonics* **11** 1327
[8] Zhang J, Zhang L, Pang X, Ozolins O and Yu X 2024 *J. Lightwave Technol.* **42** 8739

[9] Appeltant L, Soriano M C, Van der Sande G, Danckaert J, Massar S, Dambre J, Schrauwen B, Mirasso C R and Fischer I 2011 *Nat. Commun.* **2** 468
[10] Lee W W, Cho J, Hur J, Oh H and Yoo H 2025 *Nano Converg.* **12** 57
[11] Larger L, Baylón-Fuentes A, Martinenghi R, Udaltsov V S, Chembo Y K and Jacquot M 2017 *Phys. Rev. X* **7** 011015
[12] Ortín S, Soriano M C, Pesquera L, Brunner D, San-Martín D, Fischer I, Mirasso C R and Gutiérrez J M 2015 *Sci. Rep.* **5** 14945
[13] Tan S L, Wu Z M, Yue D Z, Wu W L and Xia G Q 2022 *Opt. Continuum* **1** 1593
[14] Harkhoe K, Verschaffelt G, Katumba A, Bienstman P and Van der Sande G 2020 *Opt. Exp.* **28** 3086
[15] Zhu P, Wang H and Ji Y 2025 *IEEE J. Sel. Top. Quantum Electron.* **31** 7400112
[16] Sugano C, Kanno K and Uchida A 2020 *IEEE J. Sel. Top. Quantum Electron.* **26** 1500409
[17] Chen Y, Yi L, Ke J, Yang Z, Yang Y, Huang L, Zhuge Q and Hu W 2019 *Opt. Exp.* **27** 27431
[18] Hou Y S, Xia G Q, Yang W Y, Wang D, Jayaprasath E, Jiang Z F, Hu C X and Wu Z M 2018 *Opt. Exp.* **26** 10211
[19] Jin J, Jiang N, Zhang Y, Feng W, Zhao A, Liu S, Peng J, Qiu K and Zhang Q 2022 *Opt. Exp.* **30** 13647
[20] Tavakoli S K and Longtin A 2024 *Phys. Rev. E* **109** 054203
[21] Qiu F, Bai Y, Qu D, Han L, Zhang Y, Shan G and Chen M 2023 *Laser Phys.* **33** 075001
[22] Abdulrhmann S, Alhasan A M and Madkhli A Y 2023 *Appl. Sci.* **13** 12827
[23] Zhang M J, Niu Y N, Zhao T, Zhang J Z, Liu Y, Xu Y H, Meng J, Wang Y C and Wang A B 2018 *Chin. Phys. B* **27** 050502
[24] Soriano M C, García-Ojalvo J, Mirasso C R and Fischer I 2013 *Rev. Mod. Phys.* **8**5 421
[25] Hua F, Fang N and Wang L T 2019 *Acta Phys. Sin.* **68** 224205 (in Chinese)
[26] Paquot Y, Duport F, Smerieri A, Dambre J, Schrauwen B, Haelterman M and Massar S 2012 *Sci. Rep.* **2** 287
[27] Duport F, Schneider B, Smerieri A, Haelterman M and Massar S 2012 *Opt. Exp.* **20** 22783
[28] Nakayama J, Kanno K and Uchida A 2016 *Opt. Exp*. **24** 8679
[29] Liu Q, Li P, Kai C, Hu C Q, Cai Q, Zhang J G and Xu B J 2021 *Acta Phys. Sin.* **70** 154209 (in Chinese)
[30] Uchida A, McAllister R and Roy R 2004 *Phys. Rev. Lett.* **93** 244102
[31] Hourdakis E and Trahanias P 2013 *Neurocomputing* **107** 40
[32] Roy S and Basu A 2016 *Neural Comput.* **28** 2557
[33] Jin Z, Yang J Y, Tang Z M and Hu Z S 2001 *Pattern Recognit.* **34** 2041
[34] Yue D, Wu Z, Hou Y, Cui B, Jin Y, Dai M and Xia G 2019 *Opt. Exp.* **27** 19931
[35] Tobbens A and Parlitz U 2008 *Physical Review E* **78**, 016210
[36] Lymburn T, Khor A, Stemler T, Corrêa D C, Small M and Jüngling T 2019 *Chaos* **29** 023118
[37] Choi J, Park E, Jang B and Kim Y 2023 *AIP Adv.* **13** 115110

[38] Huang Y, Zhou P, Yang Y and Li N 2021 *Opt. Lett.* **46** 6035
[39] Vinckier Q, Duport F, Smerieri A, Vandoorne K, Bienstman P, Haelterman M and Massar S 2015 *Optica* **2** 438
[40] Shen Y W, Li R Q, Liu G T, Yu J, He X, Yi L and Wang C 2023 *Optica* **10** 1745
[41] Wu Q, Zhou L, Sun X, Zhu H, Lu L and Chen J 2015 *Optics Communications* **341** 69